Low-cost multispectral vegetation imaging system for detecting leaking CO$_2$ gas

Justin A. Hogan,[1] Joseph A. Shaw,[1,*] Rick L. Lawrence,[2] and Randal M. Larimer[1]

[1]Electrical and Computer Engineering Department, Montana State University, Bozeman, Montana USA 59717

[2]Land Resources and Environmental Sciences Department, Montana State University, Bozeman, Montana USA 59717

*Corresponding author: jshaw@ece.montana.edu

As a component of a multisensor approach to monitoring carbon sequestration sites for possible leaks of the CO$_2$ gas from underground reservoirs, a low-cost multispectral imaging system has been developed for indirect detection of gas leaks through observations of the resulting stress in overlying vegetation. The imager employs front-end optics designed to provide a full 50° field of view with a small, low-cost CMOS detector, while still maintaining quasi-collimated light through the angle-dependent interference filters used to define the spectral bands. Red and near-infrared vegetation reflectances are used to compute the normalized difference vegetation index (NDVI) and spatial and temporal patterns are analyzed statistically to identify regions of anomalous stress, which are then flagged for closer inspection with *in-situ* CO$_2$ sensors. The system is entirely self-contained with an onboard compact computer and is housed in a weather-proof housing to enable extended outdoor deployment. © 2012 Optical Society of America

OCIS codes: 110.0110, 110.4234, 280.0280, 280.4788, 220.4830.

1. Introduction

Multispectral imaging of vegetation provides a convenient indirect mechanism for detecting CO$_2$ gas leaking from underground storage reservoirs. This enables long-term monitoring for site verification in geological carbon sequestration, which has been proposed as a way to reduce atmospheric emission of carbon dioxide through storage in underground features [1]. Environmental and safety concerns motivate an effective strategy for monitoring sequestration sites for signs of CO$_2$ leakage. Immediate leak detection and quantification ensures human safety by enabling rapid notification and/or evacuation of individuals in the vicinity of a leak and it allows the environmental effects to be quickly characterized. Many remote sensing and direct-measurement techniques have been proposed as viable leak detection systems. Remote sensing techniques proposed for leak detection include ground-based and airborne hyperspectral [2] or multispectral [3] imaging systems, as well as a variety of laser absorption systems [4]. Our research uses near-surface multispectral imaging of vegetation to indirectly detect the presence of CO$_2$ by tracking changes in red and near-infrared (NIR) reflectance caused by elevated gas concentrations at the vegetation root-level.

Near-surface imaging of vegetation is proposed as a technique for leak detection because it avoids cloud obscuration, provides better temporal coverage at lower cost than aerial or satellite-based imaging, and larger spatial coverage than *in-situ* measurement systems. A static instrument orientation allows direct comparison of images acquired over long periods of time. The primary disadvantage of such a system is the limited spatial coverage compared to aerial or orbital instruments. However, multiple low-cost imaging systems can be deployed in a ground-based network to monitor regions of elevated leakage risk, such as near injection wellheads or identified geological fracture zones.

The imager was designed to measure trends in red and NIR reflectance to monitor vegetation for signs of abnormal stress. Collecting this spectral information enabled use of the normalized difference vegetation index (NDVI), which is commonly used to represent vegetation health or vigor. Healthy plants exhibit low red reflectance and high NIR reflectance. Low red reflectance is caused by chlorophyll absorption as it uses the light to produce food for the plant; high NIR reflectance is caused by properties of the leaf structure and by foliage water content [5]. The rapid transition from low to high reflectance at what is known as the "red edge" occurs in the spectral vicinity of 700 nm. As vegetation becomes stressed and dies, a flattening of the reflectance spectrum is observed as visible-light reflectance increases and NIR reflectance decreases. Figure 1 depicts these properties of vegetation reflectance.

The instrument described here was developed as a lower-cost, compact replacement for an earlier proof-of-concept system that used a GeoSpatial Systems MS3100 camera and external control computer with cost in excess of $35,000 [3]. The resulting system has a wide-angle field of view (FOV) (>50° full-angle), red, and NIR spectral bands expandable to additional bands as necessary, automated data acquisition, and cost under $4000. The imager's FOV can be expanded or adjusted through the use of specially designed front-end optics that capture a wide-angle image and converts the rays to a quasi-collimated beam that passes through the strongly angle-dependent interference filters before being reimaged onto the CMOS detector.

The balance of this paper discusses the instrument design, construction, and characterization, presents example data from a field deployment to a controlled CO_2 release experiment hosted by the Zero Emissions Research and Technology Center (ZERT) in Bozeman, Montana during summer 2010, and ends with concluding remarks.
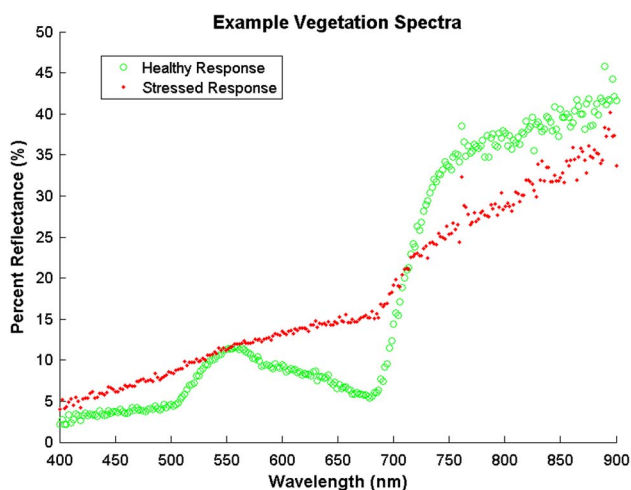

Fig. 1. (Color online) Reflectance spectra for healthy and highly stressed vegetation.

2. System Design

In our experiments, the instrument was deployed atop a 3 m scaffold and viewed the study area at a 45° downward observation angle. To image the entire vegetation study area from the scaffold required a full-angle FOV near 50°. Because this system was designed for use from a static, rather than airborne, platform, we chose to use a Thorlabs FW102B six-position rotating filter wheel populated with red and NIR interference filters to isolate the desired spectral bands (leaving four empty slots to be used for other wavelengths when needed). The use of interference filters in this system created two competing needs that drove the design of the front-end imaging optics. The first need was the wide-angle FOV, which results in the use of a very short-focal-length objective lens and consequently large ray angles between this lens and the small imaging detector array. The second need was minimum ray angles passing through the strongly angle-dependent interference filters, whose transmission bands shift to shorter wavelengths as the ray angles increase.

If the optics were not designed to minimize ray angles through the filters, the angle-dependent shift of filter transmission would result in a different center wavelength for off-axis and on-axis pixels of an image for each band. This consideration also is important from an application standpoint, as it is crucial for the center wavelength of the NIR filter to remain well above the red edge of the vegetation reflectance spectrum. As a result, it was not practical in this application to simply place the filter wheel in front of a camera. Instead, we designed an optical train to provide a quasi-collimated region in which to insert the filter wheel between the objective lens and a reimaging triplet lens immediately before the camera. This optical train employed field lenses to reduce the incidence angles of rays passing through the filters, thereby greatly minimizing the off-axis spectral shift. The full optical layout is shown in Fig. 2.

The system was based on a 1.3 Megapixel CMOS camera with 1280×1024 pixels and 6.7 μm pixel pitch. The camera communicates with a single-board computer embedded in the imager enclosure via a USB communications interface. Considerations for choosing the camera included a high-level control interface for ease of image acquisition, low-cost, and reasonable sensitivity to both red and NIR wavelengths. Although the sensor's sensitivity to light in the pass band of the NIR filter was half that of the red band, it was high enough to expect acceptable performance in this application because the NIR vegetation reflectance is so much higher than the red reflectance.

The first-order design of the front-end optics was done by using paraxial ray-trace equations to determine the powers of a field lens to be placed at the back focus of the objective lens to produce a quasi-collimated beam to pass through the interference
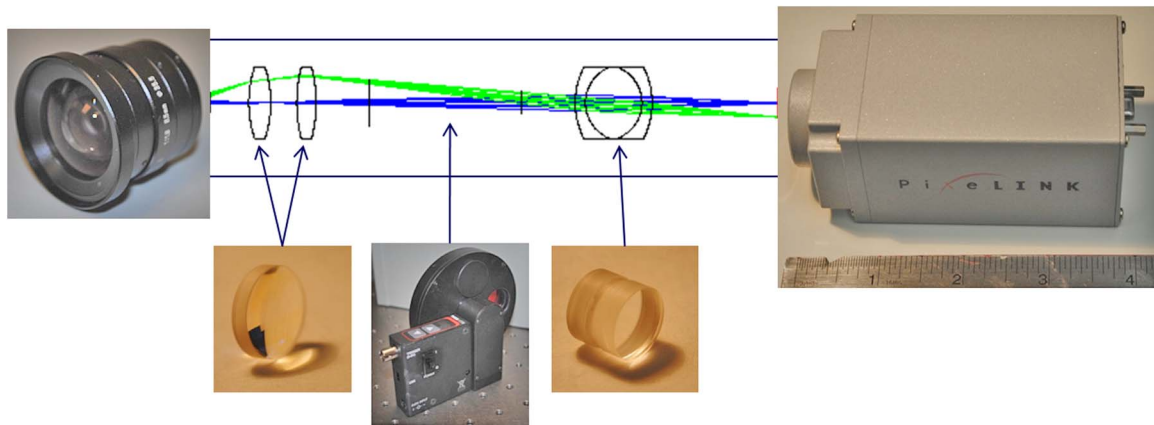
Fig. 2. (Color online) Ray-tracing model of the optical system and schematic representation of the primary components including (left-to-right) the Tamron front-end lens, the singlet field lenses, the filter wheel, the reimaging triplet, and the PixeLink camera.

filters. The C-mount objective lens was chosen based on the shortest readily available focal length, 6.5 mm, to achieve a wide FOV. This began with an estimate of the maximum ray angle exiting the objective lens, which was ~18.25° based on our observations of a focused laser beam. We solved the paraxial ray-transfer equation for the power of a single field lens that would collimate light incident on the field lens at 18.25° with a ray height of 4.285 mm (the height of the CMOS sensor). This showed that we needed a field lens of focal length 13.45 mm. However, to reduce aberrations and to provide additional adjustments in the optical layout, we split the field lens into two elements, a Thorlabs LB1014 singlet ($f = 25$ mm) and a LB1450 singlet ($f = 20$ mm), separated by about 8 mm. A triplet lens (JML TRP14350/100) with 19 mm focal length was positioned 30 mm behind the back field lens to provide room for the filter wheel to be placed in the quasi-collimated optical space.

The optical system was modeled in ZEMAX using the selected elements (Fig. 2). This model was used to provide baseline performance estimates and to gain confidence that the system could be built using the chosen components. The model yielded estimates for performance parameters such as image height at the detector, image-plane spot size, lens separations, aberrations, and filter incidence angles. A key assumption of the model was the maximum ray angle of the light exiting the Tamron front-end lens. This parameter was important because it determined the powers and placements of the field lenses. The maximum ray angle was estimated using the geometry of the lens back focal distance and the height of the camera sensor.

The optical system was constructed using a combination of half- and one-inch Thorlabs optics tubes. The field lenses and reimaging triplet were 12.5 mm diameter optics and were mounted in the half-inch tubes. The half-inch tubes housing the field lenses and reimaging triplet were mounted within one-inch optics tubes using externally threaded half-to-one-inch adapters. This allowed all the interlens spa-

cings to be adjusted. Also, the Tamron lens mounting threads, filter wheel apertures, and camera body threads more readily accepted one-inch optics tubes, so the use of one-inch tubes to house the optical elements made the overall system construction much simpler.

The interelement distances were measured using a digital caliper and were initially based on the results of the system ZEMAX design. However, primarily because of uncertainties in modeling rays from the Tamron front-end lens, this baseline configuration yielded a FOV that was too narrow for the target application. To increase the FOV, the positions of all lens elements were adjusted through a trial-and-error process until an acceptable FOV was achieved with reasonable resolution. The final image area was an 800-by-600 subset of the 1280-by-1024 pixel sensor. In the end, uncertainties in the front-end lens assembly ray angle estimates resulted in a trade-off between image resolution and system FOV. Though not ideal, sacrificing image resolution was an acceptable trade-off because of the degree of spatial averaging used in the data processing (high spatial resolution was not a key criterion in this application). In the final configuration, and before image cropping, the horizontal and vertical full-angle FOV measured 61° and 51°, respectively.

The instrument control system was automated using MATLAB software, which naturally leads to using a PC to control the instrument. However, the requirement of being field-deployable drives a low-power requirement, as it is anticipated that the system will be deployed in areas with limited power resources. A compromise between power consumption and system capabilities was found in a VIA Technologies EPIA-P700 Pico-ITX form-factor single-board computer. This small computer featured a maximum power draw of only 12 W, large data storage capacity via a 320 GB laptop hard drive, and sufficient USB ports for camera and filter wheel control.

A custom MATLAB script was written to control instrument operation. Neither the camera nor the filter wheel was natively supported by the MATLAB

software, so a small library of functions for accessing the camera's integration time, gain, sensor temperature, and image acquisition facilities was written in the C-language and interfaced with the MATLAB environment using MEX-functions. Similarly, library functions to read and set the filter wheel position were used to control spectral channel selection. The control script automated data acquisition and only relied on user input for defining the operation start time, end time, calibration target, and the interval at which images were to be acquired.

The entire system was housed in an opaque polycarbonate enclosure with a hinged, latching lid (Fig. 3) with a rubber seal. Individual system elements were mounted securely to an aluminum chassis inside the box. IP-67 rated switches and interconnect ports were chosen to populate the control computer interface panel on the outside of the enclosure. Waterproof and dustproof components provided confidence that the system would operate for multiple weeks in the field with minimal risk of damage. A square hole was cut in one side of the box and covered with a thin Lexan window through which the camera viewed the target scene. A control panel provides two plug receptacles for computer and filter wheel power, a toggle switch for disconnecting power to the entire system, momentary switches for booting and resetting the computer, an Ethernet port, and two USB connections. These external USB connections are useful for offloading data to a removable storage device or connecting additional USB peripherals, such as a CD/DVD-ROM drive for installing system software. The Ethernet port enabled remote operation of the instrument over a network connection. This capability was used extensively during the design and characterization work, as it allowed the computer to be controlled without the need for a dedicated mouse, keyboard, or monitor.
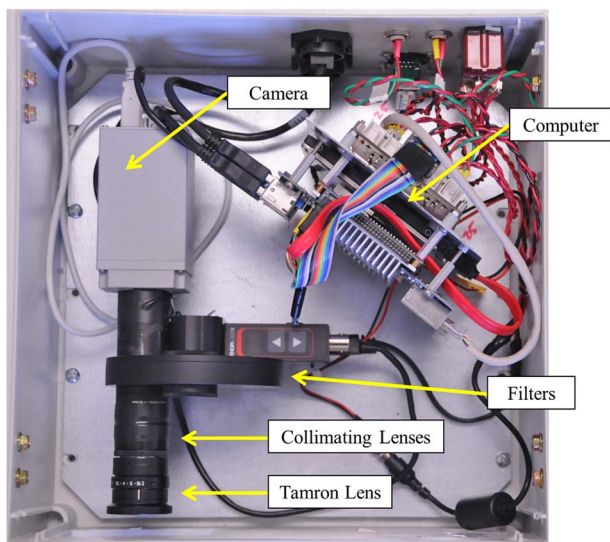

Fig. 3. (Color online) Photograph of the imaging system in its outdoor housing with the top open.

3. System Characterization

Prior to deployment to the field experiment, the imaging system underwent testing to quantify and correct for dark current noise in the CMOS sensor and geometric fall-off of light caused by the optical elements. The purpose of this was to reduce the effects of thermal and spatial noise and spatial non-uniformity in the system. Each correction was applied to every pixel of every image prior to storage and subsequent use in post processing.

A dark current correction was measured for varying internal camera temperature, gain, and integration time. A cap was placed over the front of the camera to prevent light from reaching the sensor. The camera was placed in a darkened thermal chamber capable of varying temperature through a range to exceed thermal conditions expected in the field experiment. Dark current images also were recorded for varying camera gain and integration time settings. The dark current noise values tended to increase with increasing temperature and integration time. Under typical operating conditions, the average dark current values were around 3DN or 1.2% of the full 8 bit dynamic range.

A consequence of increasing the FOV of the instrument was that only a subset of the detector pixels was illuminated. As a result, there was a circular irradiance fall-off around the edges of the image. To account for this fall-off, the FOV of the imager was uniformly illuminated using an integrating sphere and a pixel-by-pixel linear correction of the target pixel value versus the observed pixel value was calculated. The target pixel value was calculated as the mean of a 40×40 region of pixels in the center of each image. The brightness of the integrating sphere was held constant while the integration time of the camera was varied to provide a target pixel value vector between zero and 255 or the full range of the 8 bit measurement. Figure 4 shows an example of the average correction applied to a single row of pixels within the usable image region.
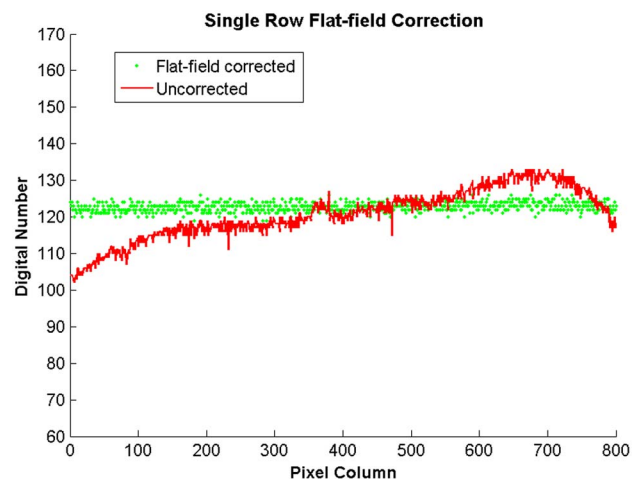

Fig. 4. (Color online) Example flat-field correction applied to a single row of pixels.

3.A. Spectral Characterization

One of the primary optical design goals was to reduce as much as possible the incidence angles on the interference filters and therefore minimize the spectral shift of the instrument response with incidence angle. It is especially important that the NIR band does not shift downward to overlap the reflectance red edge at 700 nm. For this purpose, a test was devised to measure the system on- and off-axis spectral responses using a monochromator as an illumination source and the camera CMOS sensor as the detector. This measurement covered the entire optical train of the system as deployed in the field, including the Lexan window covering the observation port, the individual optical filters, all the lenses, and the CMOS sensor.

The instrument on- and off-axis spectral responses were measured by sweeping the output wavelength of the monochromator and recording the signal observed by the imager (normalized by the spectral distribution of the monochromator lamp output and the angular transmittance of the Lexan window). Figure 5 shows the measured on- and off-axis spectral response curves for both the red and NIR filter channels. This figure shows that even at the edge of the instrument's 23° half-angle (cropped) FOV, there is very little spectral shift in the instrument response, indicating that the wide-angle front-end optical design is effective.

4. System Deployment

4.A. Experiment Overview

The prototype imager was deployed in a field experiment sponsored by ZERT, a research collaborative that seeks to advance technology related to geological carbon sequestration. ZERT research goals include development of advanced computer models to predict and understand the behavior of sequestered CO_2, development of sequestration integrity moni-
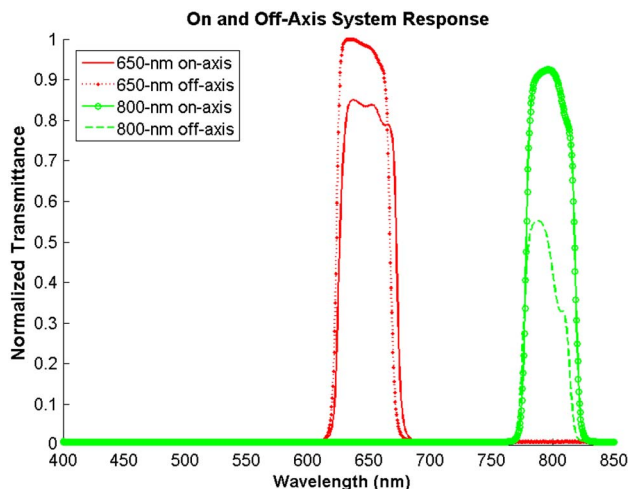
Fig. 5. (Color online) Red and near-infrared system spectral responses normalized to the off-axis red peak, demonstrating minimal spectral shift in the off-axis response.

toring technologies used for monitoring sequestration sites for signs of leakage, and development of sequestration project management strategies [6]. Primary collaboration partners include Montana State University (MSU), Los Alamos National Laboratory, Lawrence Berkeley National Laboratory, Lawrence Livermore National Laboratory, National Energy and Technology Laboratory, Pacific Northwest National Laboratory, and West Virginia University [6]. An annual controlled CO_2-release field experiment designed to test near-surface leakage detection technologies has been hosted by ZERT since 2007. This experiment is used by researchers to monitor the effects of the subsurface CO_2 release on near-surface water, soil, vegetation, and atmosphere using various measurement and observation techniques.

The ZERT field site is located at the MSU Department of Animal and Range Sciences, Bozeman Agricultural Research and Teaching Farm just west of the MSU main campus in Bozeman, Montana. The CO_2 release site is an approximately 0.35 square-km, nominally flat pasture consisting of a variety of vegetation [7]. Resident vegetation includes western salsify, dandelion, Canada thistle, alfalfa, birds-foot trefoil, clover, lupine, quackgrass, orchard grass, and Kentucky bluegrass [8]. CO_2 is released from an on-site storage tank into a 100 m horizontal injection well buried approximately 1.8 m below the surface. The release pipe is divided into six subregions, called zones, each with its own release rate control point. This division enables zone-unique release rates. The multispectral imaging system was deployed to a specific region of the test field known as the plant block, cordoned off from the rest of the field and reserved for plant research. Unlike the rest of the field, the vegetation test area remained unmown.

The plant block is approximately 400 m² and is bisected by the release pipe. A 3 m tall scaffolding housing the imaging instruments is offset approximately 3 m from the pipe and the imagers are situated such that the release pipe runs horizontally through the FOV. The scaffolding provides sufficient height for our imagers to view all the vegetation from the pipe out to the edge of the test area. This FOV purposely includes vegetation well removed from the release pipe, which is used as a reference during data processing to represent vegetation unaffected by released CO_2. The FOV also includes a region of vegetation near the release pipe that is known to be exposed to high root-level CO_2 concentrations. This region, known as a "hot spot," displays the most dramatic effects of the released CO_2 on the vegetation. Typically, by the end of a release, the CO_2 hot spots are plainly visible as nominally circular patches of completely dead vegetation. A known-reflectance Spectralon calibration target is placed in the imager FOV for use in adjusting the exposure time during image acquisition and for calculating absolute reflectance values for red and NIR images

Fig. 6. (Color online) Imaging systems mounted atop 3 m tall scaffolding at the ZERT field site. The multispectral imager is behind the left window of the white instrument housing box. The tripod in the foreground holds the reflectance calibration panel

during post processing. A photograph of the deployed equipment is shown in Fig. 6.

The imager performed well during its first deployment to a field experiment in 2010. The release spanned 27 days from July 19th to August 15th and had a release rate of 0.15 tons/day. Typical daytime temperatures at the field site during the months of June, July, and August range from 25–35 °C. Localized afternoon thunderstorms, which bring periods of high winds, heavy rainfall, and sometimes hail, are common during the deployment. The imager was configured to collect data daily at ten-minute intervals between the hours of 9 AM and 4 PM. Data collection was only interrupted by major precipitation events or power outages at the field site. There was considerable precipitation during June and into early July, but there was a dry spell through the first half of the release. Environmental conditions at the field site are not controlled and properties such as soil composition, soil moisture, sun exposure, vegetation diversity, etc. are assumed to be nominally homogeneous throughout the vegetation test area. Environmental vegetation stresses, including typical seasonal stress, are additive to the stress induced by the presence of high concentrations of CO_2 at the root-level of exposed vegetation.

The effects of the CO_2 are distinguished from naturally occurring stress effects by studying the differences between control vegetation and hot spot vegetation [3].

4.B. Example Data

Data were collected for 25 of the 27 days during which CO_2 was released. A prerelease data series of seven days provided baseline measurements for the vegetation while it was seasonally healthy and before exposure to any CO_2. The instrument also was operated for 14 days following the end of the release to observe how the vegetation responded after the CO_2 flow was terminated. By the midpoint of the release there were several discernible regions of stress within the test area. In addition to the hot spot, areas stressed by foot traffic also were present, but these were in known areas and were not included in the vegetation data analysis.

Figure 7 shows example images taken midway through the release, with the Spectralon reflectance calibration panel visible to the left and the regions stressed by elevated CO_2 flux and foot traffic to the right. As expected, the red vegetation reflectance values were generally low [Fig. 7a], with higher values observed in stressed regions. The corresponding image for NIR reflectance is shown in Fig. 7(b), with a wide variety of reflectance values arising because the scene contained shaded areas, healthy vegetation, stressed vegetation, and senesced canopy regions. Figure 7(c) is the NDVI image calculated at each pixel from Eq. (1) using the red reflectance ρ_{Red} of Fig. 7(a) and the NIR reflectance ρ_{NIR} of Fig. 7(b). NDVI values in general range from −1 to 1, with values in this image varying from about −0.4 to 0.9.

$$\text{NDVI} = \frac{\rho_{\text{NIR}} - \rho_{\text{Red}}}{\rho_{\text{NIR}} + \rho_{\text{Red}}}. \tag{1}$$

In our research we have seen NDVI values for healthy vegetation as high as about 0.8 and stressed vegetation in the area of 0.3 to 0.4. The stressed
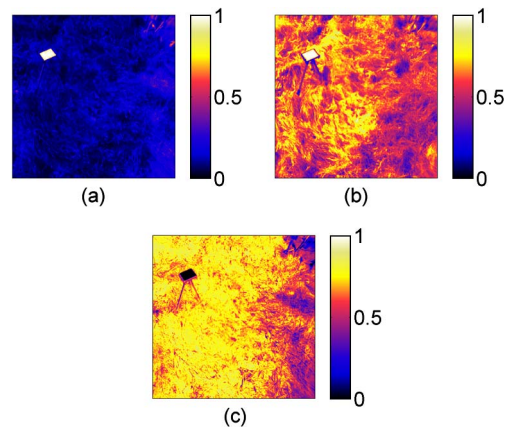

Fig. 7. (Color online) Example images from the 2010 field experiment: (a) red reflectance, (b) near-infrared reflectance, and (c) normalized difference vegetation index (NDVI).

regions were clearly visible along the right-hand-side of the NDVI image, corresponding to areas known to have experienced stress from both high CO_2 flux and human foot traffic [9]. One potential limitation of this technique is that it measures an integrated vegetation stress and cannot isolate individual stress agents such as leaking gas, water stress, or foot traffic [3,9]. However, the system can be used to identify stressed vegetation regions that can be examined in more detail with a point sensor that directly measures the leaking gas.

A full analysis of the 2010 field experiment data used time-series analysis to show that reflectance and NDVI changes throughout the experiment were correlated with root-level CO_2 exposure and were distinguishable from changes associated with seasonal factors such as precipitation, wind, temperature variations, and so forth [9,10]. The complete analysis includes depiction of time-series trends of the reflectance and NDVI data for CO_2-affected plants versus control vegetation, as well as a multiple linear regression (MLR) model derived from combined reflectance and NDVI values. The vegetation imaging method was able to detect CO_2-induced changes within approximately two-to-three days of the initiation of the leak, well before the vegetation was affected to the degree that it would be visible by eye.

5. Conclusions

A low-cost multispectral imaging system was designed, built, calibrated, and deployed to a controlled, subsurface carbon dioxide leak experiment. An environmentally robust system was built using off-the-shelf components. The system employs interference filters to isolate red and NIR spectral bands for use in monitoring vegetation stress through the NDVI. To avoid spectral shifts of the instrument response for off-axis pixels, a specially designed front-end optics module was designed to create a region of quasi-collimated light between the wide-angle objective lens and the CMOS detector array. This optical design resulted in a wide-angle FOV ($\sim$50°) with nearly constant spectral response all the way to the edge of the field.

Network-controlled operation and data transmission has been demonstrated by operating the instrument via the Windows operating system's remote desktop facilities. The instrument was designed to acquire and store data over long periods of time, making it ideal for extended deployments. Future design work will focus on system miniaturization and further power and cost reduction by moving from a desktop computer environment to a dedicated embedded system that acquires image data and relays it off-site for storage and processing.

This compact imager design can be useful for leak detection at carbon sequestration sites if multiple imagers are employed with maximal FOV to monitor large areas. This kind of system may be most useful for monitoring areas prone to elevated leakage risks —for example, near injection wellheads or identified

geological fracture zones. Incorporating network communication capabilities into the systems allows interinstrument communication and data relay to a base station for analysis. A distributed network configuration allows the instruments to be operated by solar power and reduces the distance signals must be transmitted at a given time. Data can be relayed from system to system en route to a central processing center. Analysis of incoming data can be performed to identify areas exhibiting abnormal reflectance characteristics. These areas of interest can be flagged for subsequent inspection using *in-situ* measurement techniques to verify the presence of leakage. Areas flagged for inspection are those which exhibit reflectance variations outside ranges attributable to seasonal or environmental influences as determined by observations of vegetation in the vicinity of the suspect region.

A targeted deployment of near-surface imaging systems to specific areas at a sequestration site that are identified as likely leak spots through analysis of the geological properties of the storage feature will be the most feasible and cost-effective deployment strategy. A network of these low-cost imagers may provide a convenient method of monitoring large areas above carbon sequestration sites (tens of meters to a few kilometers). However, use of this system is only practical in areas covered with grassy vegetation and, therefore, only during seasons when vegetation is growing. This system could also be used in other applications requiring detection of gas leaking from underground or even detection or measurement of vegetation stress by other causes.

References

1. S. J. Friedmann, "Geological carbon dioxide sequestration," Elements **3**, 179–184 (2007).
2. C. J. Keith, K. S. Repasky, R. L. Lawrence, S. C. Jay, and J. L. Carlsten, "Monitoring effects of a controlled subsurface carbon dioxide release on vegetation using a hyperspectral imager," Int. J. Greenhouse Gas Control **3**, 626–632 (2009).
3. J. H. Rouse, J. A. Shaw, R. L. Lawrence, J. L. Lewicki, L. M. Dobeck, K. S. Repasky, and L. H. Spangler, "Multi-spectral imaging of vegetation for detecting CO_2 leaking from underground," Environ. Earth Sci. **60**, 313–323 (2010).
4. J. L. Barr, S. D. Humphries, A. N. Nehrir, K. S. Repasky, L. M. Dobeck, J. L. Carlsten, and L. H. Spangler, "Laser-based carbon dioxide monitoring instrument testing during a 30-day controlled underground carbon release field experiment," Int. J. Greenhouse Gas Control **5**, 138–145 (2011).
5. E. A. Walter-Shea and J. M. Norman, "Leaf optical properties," in *Photon-Vegetation Interactions: Applications in Plant*

Physiology and Optical Remote Sensing, R. B. Myneni and J. Ross, eds. (Springer-Verlag, 1991), pp. 230–251.

6. Montana State University, "Zero Emissions Research and Technology: A National Resource For Geologic Sequestration Science," http://www.montana.edu/zert/index.html.

7. L. H. Spangler, L. M. Dobeck, K. S. Repasky, A. R. Nehrir, S. D. Humphries, J. L. Barr, C. J. Keith, J. A. Shaw, J. H. Rouse, A. B. Cunningham, S. M. Benson, C. M. Oldenberg, J. L. Lewicki, A. W. Wells, J. R. Diehl, B. R. Strazisar, J. E. Fessenden, T. A. Rahn, J. E. Amonette, J. L. Barr, W. L. Pickles, J. D. Jacobson, E. A. Silver, E. J. Male, H. W. Rauch, K. S. Gullickson, R. Trautz, Y. Kharaka, J. Birkholzer, and L. Wielpolski, "A shallow subsurface controlled release facility in Bozeman, Montana, USA, for testing near surface CO_2 detection techniques," Environ. Earth Sci. **60**, 227–239 (2010).

8. E. J. Male, W. L. Pickles, E. A. Silver, G. D. Hoffman, J. L. Lewicki, M. Apple, K. S. Repasky, and E. A. Burton, "Using hyperspectral plant signatures for CO_2 leak detection during the 2008 ZERT CO_2 sequestration field experiment in Bozeman, Montana," Environ. Earth Sci. **60**, 251–261 (2010).

9. J. A. Hogan, "Multi-spectral imaging of vegetation for CO_2 leak detection," M.S. thesis (Department of Electrical and Computer Engineering, Montana State University, 2011), http://etd.lib.montana.edu/etd/view/item.php?id=1255.

10. J. A. Hogan, J. A. Shaw, and R. L. Lawrence, "Detection of leaking CO_2 gas with vegetation reflectances measured by a low-cost multispectral imager," submitted to IEEE J. Selected Topics Appl. Earth Obs. Rem. Sens.